The role of oxygen and titanium related defects on the emission of TiO$_2$:Tb^{3+} nano-phosphor for blue lighting applications

Vinod Kumar [a,*], O.M. Ntwaeaborwa [a], J. Holsa [b,c,d], D.E. Motaung [e], H.C. Swart [a,*]

[a] Department of Physics, University of the Free State, Bloemfontein ZA9300, South Africa
[b] Instituto de Química, Universidade de São Paulo, São Paulo, SP, Brazil
[c] Department of Chemistry, University of Turku, FI-20014 Turku, Finland
[d] Turku University Centre for Materials and Surfaces (MatSurf), Turku, Finland
[e] DST/CSIR National Centre for Nano-Structured Materials, Council for Scientific and Industrial Research, Pretoria 0001, South Africa

ABSTRACT

A series of terbium doped TiO$_2$ (TiO$_2$:Tb^{3+}) nanophosphors (NPr) were synthesized by the solution combustion method with varying the concentration of Tb^{3+}. The X-ray diffraction results confirmed that the polycrystalline tetragonal structure of TiO$_2$ NPr was formed. The X-ray photoelectron spectroscopy and electron paramagnetic resonance measurements confirmed the presence of oxygen and Ti^{3+} defects. The blue emission from the TiO$_2$:Tb^{3+} NPr was tuned when the concentration of Tb^{3+} was varied. These TiO$_2$:Tb^{3+} NPr have potential applications as sources of blue light in light emitting devices.

© 2015 Elsevier B.V. All rights reserved.

1. Introduction

Titanium dioxide (TiO$_2$) is one of the most important nano-materials, which have attracted attentions due to its unique properties. TiO$_2$ is a very interesting UV absorbing material not only from a scientific point of view but also due to its technological applications in dye sensitized solar cells, pigments, dielectric materials in capacitors, etc. [1–3]. TiO$_2$ has also been one of the most investigated engineering materials during the recent decades, especially in the area of energy and environmental applications. The momentum of this research and its historical development has been significantly impacted by two milestone research reports in 1972. In 1972, Fujishima et al. reported the finding of photocatalytic splitting of water on a TiO$_2$ electrode under ultraviolet (UV) light [3–5]. The discovery of this phenomenon spurred a tremendous amount of research related to TiO$_2$ photocatalysis including solar fuels and environmental remediation. Secondly, and also in 1972, Tributsch demonstrated the idea of a dye-sensitized solar cell (DSSC), fabricating a chlorophyll-sensitized zinc oxide (ZnO) electrode to convert visible light radiation into an electric current

by charge injection from the excited dye molecules into the wide band gap metal oxide [3–5]. Although in this first DSSC concept report the author used ZnO, not TiO$_2$, as the wide band gap semiconductor but TiO$_2$ was soon to become the most popular wide band gap semiconductor material for later DSSCs, mainly due to its better photostability. Considering the relatively wide band gaps (3.0 eV for rutile and 3.2 eV for anatase) [6], high refractive indices (n = 2.52 for anatase phase and n = 2.76 for rutile phase) and lower phonon energy (<700 cm^{-1}) [7], TiO$_2$ is a good candidate to be used as the host material of rare earth (RE) in order to excite RE ions efficiently and to yield intense luminescence. There has been a large uncertainty over the band gap energies for both rutile and anatase. Most studies agreed, however, that the optical absorption edges correspond to an indirect band gap, whereas a symmetry-forbidden direct gap lies close in energy [8]. Optical absorption studies suggested the opposite nature of exciton states (self-trapped or free) in anatase and rutile. For rutile, resonant measurements demonstrated the strong exciton–phonon interaction by observing a sharp resonance in the phonon scattering efficiencies. For anatase, however, no resonant Raman study has been reported at the fundamental absorption edge. Electron–phonon interaction plays a crucial role in the carrier transport in TiO$_2$ through phonon-assisted polaron hopping as well as through scattering of carriers by optical phonons [8]. Photoluminescence (PL)

* Corresponding authors.
  E-mail addresses: vinod.phy@gmail.com (V. Kumar), swarthc@ufs.ac.za (H.C. Swart).

spectroscopy is an important technique for studying the properties of semiconducting nano-particles based systems, because of its ability to investigate carrier recombination processes and energy level distributions. The later ability is especially useful investigating a variety of applications of TiO$_2$ nanophosphors (NPr). In fact, spatial and energetic distribution of intra-gap defect states influences the performances of TiO$_2$ in luminescence, photocatalysis and solar energy conversion, by limiting recombination and carrier transport [9–12]. However, it is worth noting that the interpretation of the PL process in TiO$_2$ nanostructures is relatively difficult. The diverse nature of the excitonic states associated with the different TiO$_2$ crystal phases (self-trapped excitons (STE) in anatase and free excitons in rutile) [13], leads to different excitonic PL emission bands [14,15]. The recurring green PL band, which is a signature of TiO$_2$ NPr, is commonly attributed to both STE recombination and surface radiative recombination [16–18]. These processes give very similar spectra and, owing to this similarity, the analysis of the green TiO$_2$ luminescence still remains a complicated task. Furthermore, other emission bands lying in the blue [19], red [20], and near-infrared (NIR) [21] range of the optical spectrum have been reported in TiO$_2$ nanocrystals. Different hypotheses have been proposed to explain the origin of these various emission bands, but there are still some controversies. TiO$_2$ has also demonstrated the possibility to be a good sensitizer to absorb primary excitation energy and transfer it to RE dopant ions. Semiconductors doped with RE elements such as Eu, Er, Tm, and Tb have been intensively pursued because of their important applications in optoelectronics as emitters at visible wavelengths [22]. There are two main factors leading to the stable and sharp luminescence in RE elements: one is that the 4f orbital of RE ions is shielded by the outer 6s, 5p and 5d orbitals, which weakens its coupling with the surrounding ligands; the other is that the f–f transitions are parity forbidden, resulting in small absorption cross sections [23]. The initial efforts of incorporating RE ions into Si and other narrow band gap semiconductors hindered by solubility constraints and the thermal quenching [24,25]. RE doped TiO$_2$ have been investigated most frequently, it found applications in sensors, spin light emitting diodes and non-volatile memory devices, optoelectronics, and photocatalysis [26–28].

In this paper, the effect concentration of the Tb^{3+} on the structure, particle morphology, chemical and PL properties of TiO$_2$:Tb^{3+} NPr is reported. The chemical and electronic states of TiO$_2$:Tb^{3+} were determined by X-ray photoelectron spectroscopy (XPS), while the optical properties were analysed from the UV–vis absorption and PL emission spectroscopy data. Additionally, a doping mechanism of Tb^{3+} ions in TiO$_2$ has been proposed and explained with the help of a schematic diagram. The novelty of the present work is the capability to tune the blue colour with changing the Tb^{3+} concentration.

2. Experimental technique

TiO$_2$:Tb^{3+} NPr with different doping concentration of Tb were synthesized using the solution combustion method. Titanium oxysulfate and urea were mixed and dissolved in distilled water. Terbium nitrate pentahydrate was used as the Tb source in the solution. The concentration of Tb was varied from 0 to 6 mol%. A homogeneous solution was obtained after stirring for 1 h at 80 °C. The solution was transferred to a pre-heated muffle furnace maintained at a temperature of 600 ± 10 °C. All the liquid evaporated and a large amount of heat was released which resulted into a flame that decomposed the reagents further and released more gases. The flame lasted for ~60 s and the combustion process was completed within 5 min. The resulting TiO$_2$:Tb^{3+} NPr powders

were cooled down to room temperature and ground gently using a pestle and mortar.

The crystal structure was analysed by using an X-ray diffractometer (XRD) (PAN analytical X'pert PRO). The TiO$_2$ samples were performed using Jeol JSM-7800F Field Emission Scanning Electron Microscope (FE-SEM). The XPS analysis was carried out with a PHI 5000 Versaprobe-Scanning XPS Microprobe before sputtering and after sputtering with 30 s of Ar$^+$ ions. UV–Vis absorption spectra of TiO$_2$ were recorded using a Perkin Elmer Lambda 950 UV–vis at room temperature in the range of 300–800 nm. The PL excitation and emission spectra were recorded by the Hitachi fluorescence spectrometer (F-2500). The microwave absorption measurements of the TiO$_2$:Tb^{3+} samples were carried out using a JEOL X-band electron paramagnetic resonance (EPR) spectrometer (JES FA 200) equipped with an Oxford ESR900 gas-flow cryostat and a temperature controlled (Scientific instruments 9700). The microwave power was varied between 1 and 30 mW, and the frequency was kept at approximately 9.4 GHz. The DC field was modulated with a superposed AC field with constant amplitude. The microwave response was measured as a derivative signal.

3. Results and discussion

3.1. Structure and surface morphology

The XRD patterns of TiO$_2$:Tb^{3+} NPr with different concentrations of Tb are shown in Fig. 1(a). In all the spectra, the peak positions and their relative intensities are consistent with the standard powder diffraction patterns of anatase TiO$_2$ (ICSD card # 9852). The most intense diffraction peak at 25.2° corresponds to the (1 0 1) plane. The diffraction peak position at 37.7, 47.8, 54.1, 62.5 and 69.4 are in accordance with the TiO$_2$ anatase phase [29,30]. The XRD results revealed that the powder NPr consisted of single-phase polycrystalline tetragonal structures. No other polymorph of titania was observed and no rare earth related (Tb^{3+}) peaks were found in the XRD patterns, it is believed that the Tb^{3+} occupied the Ti^{4+} sites or interstitial sites in the TiO$_2$. The RE ion was coordinated to one ligand. Tong et al. reported that to observe near-infrared luminescence in the corresponding Nd^{3+} and Er^{3+} complexes, dibenzoylmethane had to be added as a coligand to exclude water molecules from the first coordination sphere of the lanthanide ion [31]. The crystallite sizes of the TiO$_2$:Tb^{3+} NPr were calculated by Debye–Scherer's formula [32]

$$D = \frac{k\lambda}{\beta \cos\theta} \tag{1}$$

where D is the size of the crystallites, λ is the wavelength of Cu kα radiation (0.1514 Å), k is correlation factor (0.94), β is full with at half maxima (FWHM) of peak and θ is Bragg's diffraction angle. The crystallite size has varied from 16 ± 2 to 23 ± 2 nm with varying the doping concentration of Tb^{3+}. SEM images of the TiO$_2$:Tb^{3+} for 3 mol% doping concentration of Tb is shown in Fig. 3. The SEM image shows a clear network of spherical nanostructures with some degree of faceting. SIMS results (not shown) indicated that the Tb was homogeneously distributed throughout the host material. The samples obtained were also reproducible.

3.2. XPS analysis

The de-convoluted XPS spectra of the Ti 2p recorded from samples with different concentrations of Tb^{3+} before and after sputtering with Ar$^+$ are shown in Fig. 2(a) and (b), respectively. All the Ti 2p spectra show a doublet, whose binding energies are 459.1 and 464.8 eV, which can be ascribed to the Ti-2p3/2 and Ti-2p1/2 lines.
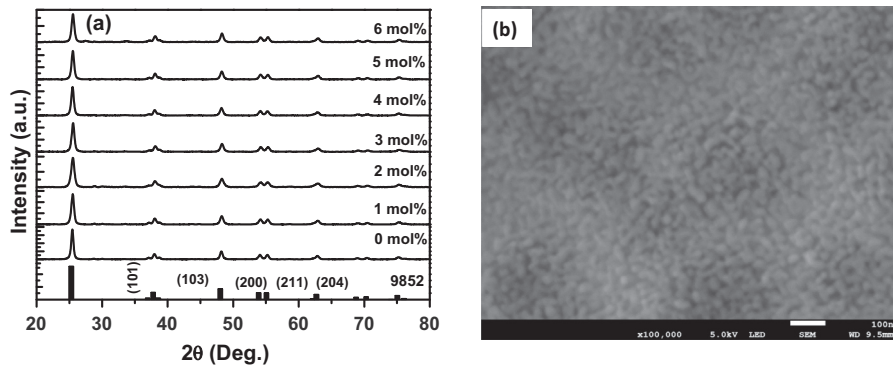
Fig. 1. (a) XRD patterns of TiO$_2$:Tb^{3+} NPr at different doping concentration, (b) the SEM image of the 3 mol% Tb^{3+} doped TiO$_2$.

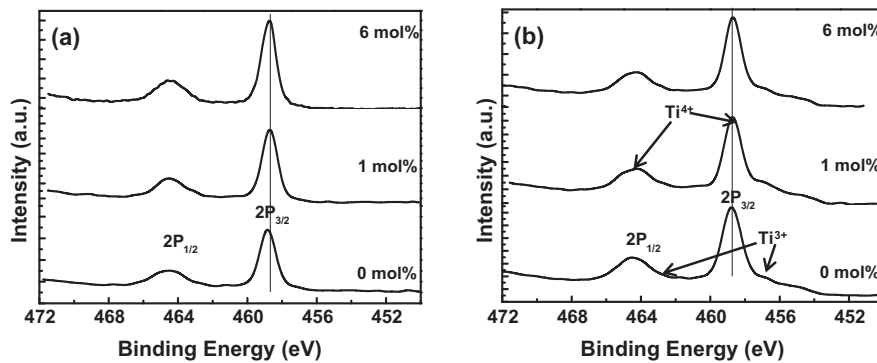**Fig. 2.** High-resolution XPS spectra of the Ti 2p core levels for 0, 3 and 6 mol% doping of Tb in the TiO$_2$:Tb^{3+} NPr (a) before sputtering, (b) after 30 s sputtering.

The binding energy difference between the two lines is 23.1 eV, which is comfortably lying close to the standard reference value of TiO$_2$ [33]. The values of the binding energy and binding energy difference show that the Ti atoms are in the Ti^{4+} oxidation state. The Ti2p photoelectron peaks are asymmetrical at the lower binding energy side of the peaks. The position of the Ti2p$_{3/2}$ peak at 459.1 eV and the shoulder at 458.0 eV indicate the presence of Ti^{4+} and Ti^{3+} oxidation states [34–36]. After sputtering, the peaks are clearly asymmetrical as shown in the 2P$_{3/2}$ peaks at the lower energy side in Fig. 2(b). This asymmetrical peak is attributed to Ti^{3+}. It must be pointed out that the sputtering may also create extra defects in the TiO$_2$, but a small shoulder peak is seen on the un-sputtered undoped sample spectrum as well.

The de-convoluted oxygen O1s peaks for the 0, 3 and 6 mol% doping of Tb in TiO$_2$:Tb^{3+} NPr is shown in Fig. 3. The high resolution spectra of the O1s peaks were measured before and after sputtering with Ar$^+$ ions for 30 s. The TiO$_2$, O1s peak is de-convoluted into three peaks, namely O1, O2 and O3. The O1 peak assigned to oxygen bound to the tetravalent Ti ions array, surrounded by Ti atoms with their full complement of nearest neighbour O^{2-} ions [37,38] The O2 peak is associated with O^{2-} ions that are in oxygen deficient regions within the matrix of TiO$_2$; such as Ti(OH)$_3$ [38,39] The O3 peak is usually attributed to chemisorbed species (such as CO$_3$, adsorbed H$_2$O or O$_2$) on the surface of the TiO$_2$ [39–41]. The intensity of the O3 peak has decreased after sputter cleaning due to the removal of surface contaminants. It must also be pointed out that the defect contribution of these spectra is very much different and different PL emission for each of these samples is therefore expected. The defect level peak (O2) of O 1s is observed to increase up to 3 mol% and after that it decreased at 6 mol%. The effect of doping on the peak position and area of the O1s peak is listed in Table 1. The maximum area of the O2 peak is observed for the 3 mol% doping of Tb. The maximum oxygen related defect

is observed for 3 mol% doping of Tb in TiO$_2$:Tb^{3+} NPr. Kumar et al. [40,41] reported that O2 related defects in oxygen 1s peak can influence the luminescence properties of ZnO and SnO$_2$ NPr due to different kinds of oxygen related defects presented in the material.

The high-resolution scans of Tb 3d$_{5/2}$ and Tb 3d$_{3/2}$ are shown in Fig. 4. The XPS peaks of Tb 3d$_{5/2}$ and 2d$_{3/2}$ were observed at 1241.2 and 1276.3 eV, respectively. An additional peak is observed at 1251 eV and it can be attributed to photoemission peaks from the energy loss structure [42]. No Tb$_2$O$_3$ peak is observed with Tb doping.

3.3. EPR measurements

Electron paramagnetic resonance (EPR) provides a sensitive and direct method to monitor behaviour caused by the presence of native defects, such as oxygen and zinc vacancies. To date, most of the experimental investigations of oxygen vacancies in TiO$_2$ have relied on EPR measurements. Fig. 5 shows the derivative of the microwave absorption (dP/dH) as a function of magnetic flux density (DC field) in TiO$_2$ NPr recorded at room temperature (T = 293 K) and microwave power of P = 1 mW. The high magnification of central part of graph is shown in the inset of Fig. 5 for calculation of g-factors. We observed two main g factor values as 2.089 and 1.995 for the undoped and 1 mol% Tb doped TiO$_2$ NPr, attributed to O$^-$ and Ti^{3+} ions [43].

The Ti^{3+} defects can be generated by reduction of the Ti^{4+} ions. The process for Ti^{4+} reduction to Ti^{3+} is dependent on the Ti^{4+} ions that receive a photoelectron. The photo generated electrons and holes are produced in the TiO$_2$. The electrons can be trapped and tend to reduce Ti^{4+} cations to the Ti^{3+} state, and the holes oxidize O^{2-} anions to form O$^-$ trapped hole or even oxygen gas [44]. The charge transfer steps are as follows:
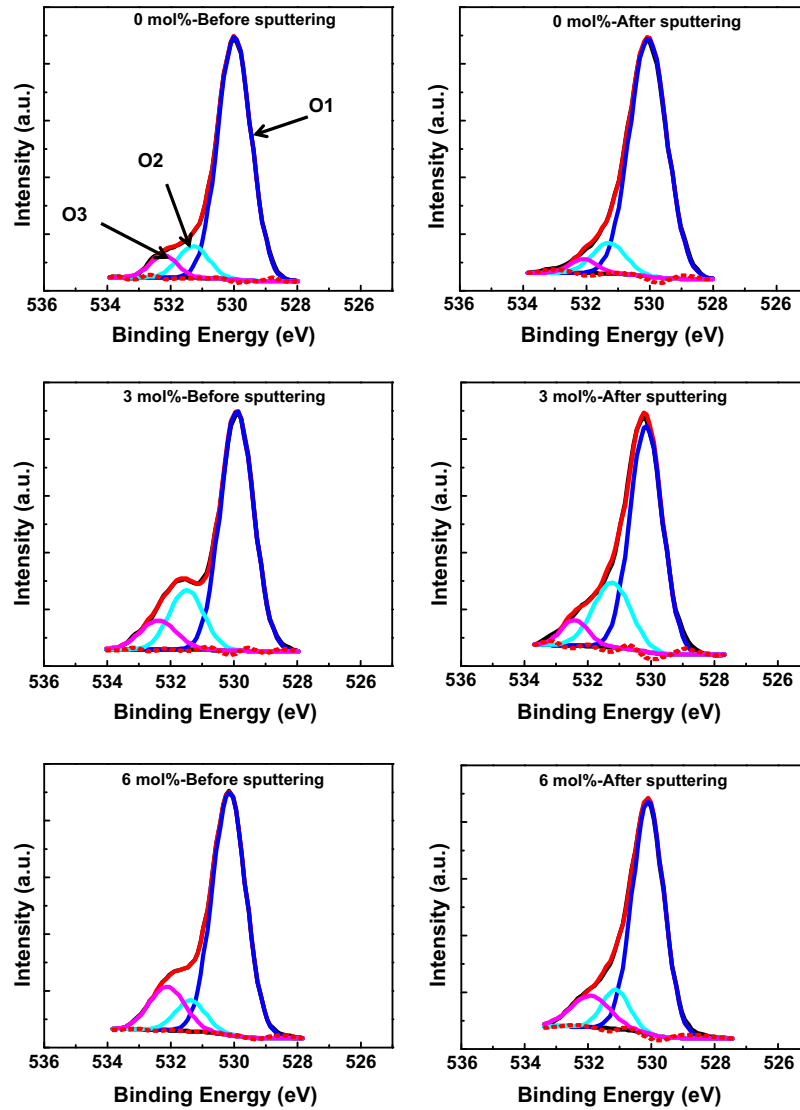
Fig. 3. De-convolution of the oxygen 1S peak of 0, 3 and 6 mol% doping of Tb before and after sputtering.

Table 1
Peak positions and areas of the different O1s peaks.

Sample (mol%)	Peak name	Before sputtering		After sputtering	
		Peak position (eV)	Area (%)	Peak position (eV)	Area (%)
0	O1	530.1	83.6	530.19	86.5
	O2	531.4	10.0	531.3	9.9
	O3	532.3	6.4	532.15	3.5
3	O1	530.0	71.9	530.1	70.2
	O2	531.4	18.5	531.25	23.2
	O3	532.4	9.6	532.45	6.7
6	O1	530.1	76.5	530.1	76.2
	O2	531.4	8.9	531.15	11.1
	O3	532.2	14.7	532.1	12.7

$$TiO_2 + hv \rightarrow e_{CB}^- + h_{VB}^+ \tag{2}$$

$$e_{CB}^- + Ti^{4+} \rightarrow Ti^{3+} \text{ Trapped electron} \tag{3}$$

$$h_{VB}^+ + O_2 \rightarrow O^- \text{ Trapped hole} \tag{4}$$

$$4h_{VB}^+ + 2O_2^- \rightarrow O_2 \tag{5}$$

3.4. Reflectance and bandgap analysis

The reflectance graph of Tb doped TiO_2 NPr with different doping concentration are shown in Fig. 6(a). A sharp band edge is observed at ~370 nm, which can be assigned to the intrinsic band-gap absorption of TiO_2 and is attributed to the electron transitions from the valence band to the conduction band ($O_{2p} \rightarrow Ti_{3d}$). A small peak is observed in the reflectance curve at ~500 nm. This peak may be due to the electron transition from the valance band to the Ti^{3+} defect level, created by UV exposure. The optical band gap of TiO_2 is estimated by the extrapolation of the linear portion of the $(\alpha hv)^2$ versus hv plots. The band gap is calculated by the Tauc's plot method [45]

$$(\alpha hv)^2 = (hv - E_g) \tag{6}$$

where A is a constant, E_g is the optical band gap, h is Plank's constant and a is the absorption coefficient. The plots of $(\alpha hv)^2$ versus hv for different TiO_2 NPr are shown in Fig. 6(b). The energy of the lowest phonon-assisted indirect allows transition from the valance band to the conduction band for TiO_2 is reported at 2.91 eV [46]. The band gaps of the TiO_2:Tb^{3+} NPr calculated by Tauc's plot method were observed in the range of ~3.36 to 3.42 eV. The band
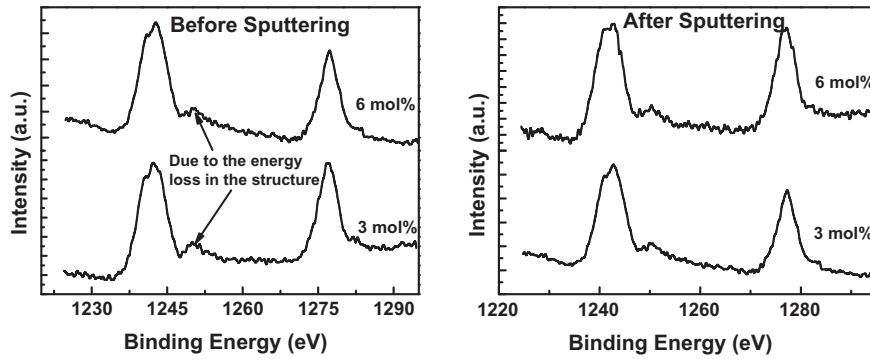
Fig. 4. De-convolution of Tb 3d peak of 3 and 6 mol% doping of Tb.
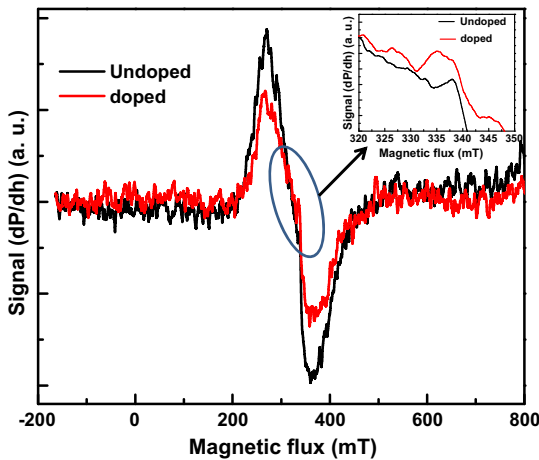

Fig. 5. EPR spectra of undoped and doped TiO_2 NPr. The magnify part of is shown in the inset.

gap can be assigned to the overlapping of the lowest energy fundamental absorption and absorption by different defects states such as Ti^{3+} or oxygen vacancies [46]. The observed bandgap in this case was higher than the band gap of bulk TiO_2 of 3.2 eV [47]. According to the XRD results, the crystalline size has varied from 16 to 23 nm with varying the doping concentration of Tb^{3+}, which is much higher than the exciton Bohr radius of TiO_2 (1.5 nm) [48]. Therefore, the effect of quantum confinement on the band gap of TiO_2 can be neglected. It is suggested that the increase in excitation energy might resulted from the coupling of the exciton to phonon (as discussed in the introduction part), which has been observed in other nanocrystalline systems [49].
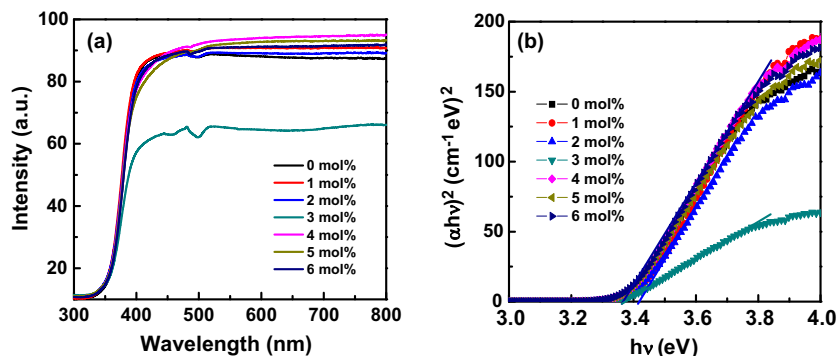
3.5. Photoluminescence emission

The spectral components of the PL measurements can provide valuable information concerning the type of defects and impurities in semiconductors, while the overall PL intensity is determined by the quantum efficiency of the material together with the surface recombination velocity. The excitation spectra measured at the emission wavelength of 543 nm of the TiO_2:Tb^{3+} NPr with different doping concentration are shown in Fig. 7(a). The excitation spectra show a broad band in the range 360–390 nm representing the inter-band transitions of the host lattice. For undoped TiO_2 the excitation peak measured at an emission of 443 nm is going up continuously due to the defect related emission in the range of 410–500 nm. The peak at 384 nm in the excitation graph of the doped TiO_2 is attributed to the $^5D_3$–$^7F_5$ transition in the Tb^{3+} [50]. The emission spectra of the TiO_2:Tb^{3+} NPr excited by 384 nm is shown in Fig. 7(b). The fluorescence PL spectra emission of TiO_2:Tb^{3+} are characterized by two different types of transitions, the one is due to defect level emission and the other one to the Tb^{3+} f–f transitions. The defect related peak is attributed to the Ti^{3+} defect as well as oxygen related defect such as the single ionized oxygen defect. The intensity of the defect related peak has increased up to a doping concentration of 3 mol% thereafter it decreased. There is a correlation between these defect related emissions and the XPS results. For the emission due to the Tb^{3+} ions, a major green emission peak at 543 nm and a few minor peaks at 489, 586 and 622 nm were detected. These peaks represent the $^5D_4$–$^7F_5$, $^5D_4$–$^7F_6$, $^5D_4$–$^7F_4$ and $^5D_4$–$^7F_3$ transitions of Tb^{3+}, respectively [51,52]. The intensity of the Tb^{3+} peaks has increased continuously with an increase in the Tb concentration. Fig. 7(c) presents the de-convoluted PL emission curve of the TiO_2:Tb^{3+} NPr for 3 mol% doping of Tb. Three defects related peaks and one Tb^{3+} peak are observed at 442, 463, 493 and 543 nm, respectively.

Fig. 6. (a) Reflectance curve of TiO_2:Tb^{3+} NPr with different doping concentration of Tb, (b) band gaps calculated with Tauc's plot method.
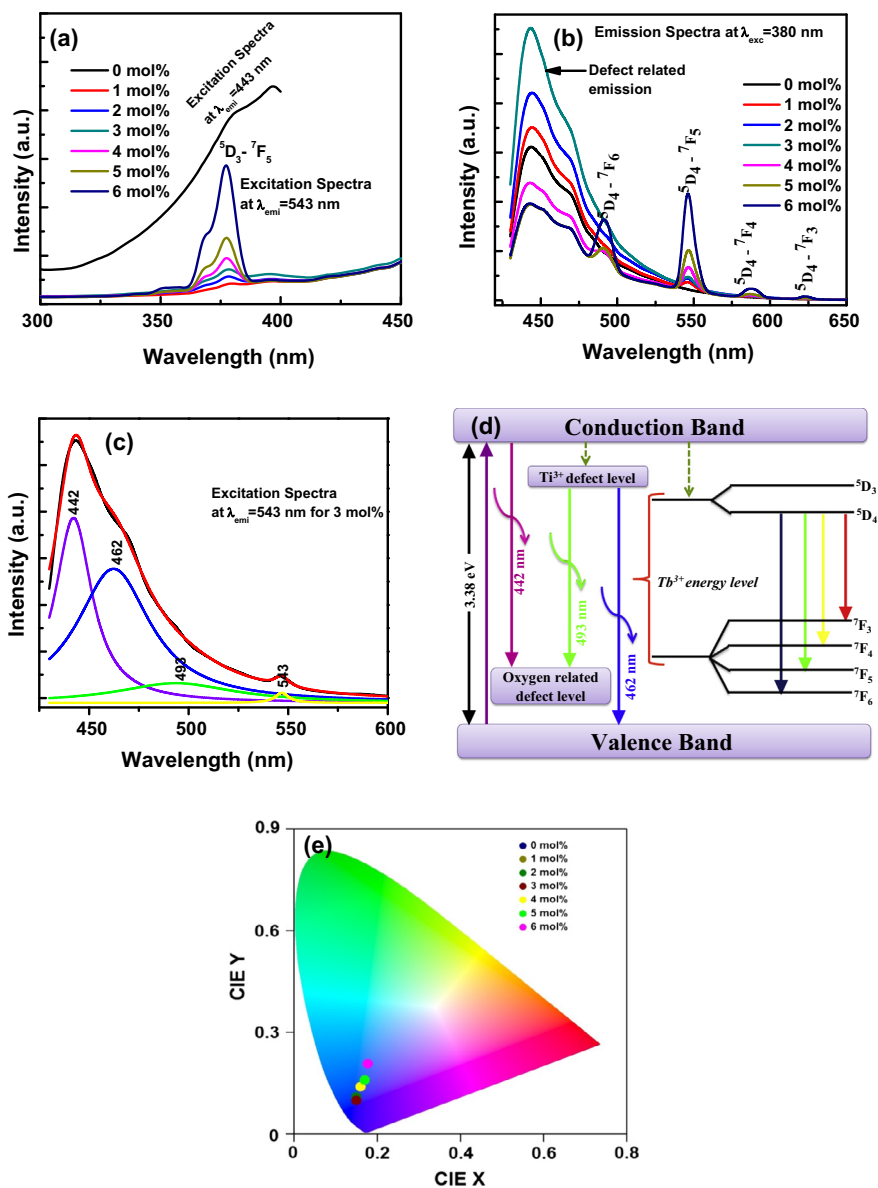
Fig. 7. (a) PL excitation curve recorded at 543 nm for different Tb concentration and at 443 nm for undoped TiO$_2$, (b) the emission graph of TiO$_2$:Tb^{3+} with different concentration of Tb, (c) the de-convoluted PL emission curve for 3 mol% doping of Tb, (d) schematic of the energy level diagram of TiO$_2$:Tb^{3+}, (e) CIE diagram of the TiO$_2$:Tb^{3+} NPr for different Tb^{3+} concentrations.

The Ti^{3+} and oxygen related defect (O$_D$) is responsible for the 442, 463 and 493 emission. To understand more about the emission in TiO$_2$:Tb^{3+} NPr, the simplified schematic band diagram is shown in Fig. 7(d). The position of the Ti^{3+} defect level is below the conduction band [53]. The oxygen related defect is just above the valence band. The band transitions from conduction band to O$_D$, Ti^{3+} to valance band and Ti^{3+} to O$_D$ result in emission at 442, 463 and 493 nm wavelengths, respectively.

The CIE (International Commission on Illumination) chromaticity diagram of TiO$_2$:Tb^{3+} NPr for different Tb^{3+} concentrations is presented in Fig. 7(e). From the chromaticity diagram, it can be seen that the colour coordinates traverse a wide range from the deep blue to light blue when the concentration of Tb^{3+} was varied. The results show that the tuning of the blue emission colour is possible by varying the Tb^{3+} concentration in the TiO$_2$ host. It is therefore clear that the TiO$_2$:Tb^{3+} NPr may be used as a blue emitting source that can easily be excited with a 380 nm semiconductor chip.

4. Conclusion

The Tb doped TiO$_2$ NPr showed emission bands in the blue and green regions attributed to the presence of Ti^{3+} and oxygen defects as well as the emission from Tb^{3+} transitions. The formation of different kind of defects was confirmed by XPS and EPR measurements. The emitting colour could easily be tuned in the blue region by varying the Tb^{3+} concentration. The TiO$_2$:Tb^{3+} NPrs belong to one kind of novel optical materials as a promising future candidate for strong blue emission and have drawn an increasing amount of attention.

References

[1] B. Oregan, M. Gratzel, Nature 353 (1991) 737.
[2] M.E. Berenson, Color Res Appl. 9 (2) (1984) 98.
[3] L. Sang, Y. Zhao, C. Burda, Chem. Rev. 114 (2014) 9283.
[4] A. Fujishima, K. Honda, Nature 238 (1972) 37.
[5] H. Tributsch, Photochem. Photobiol. 16 (1972) 261.
[6] M.A. Fox, M.T. Dulay, Chem. Rev. 93 (1993) 341.
[7] C. Urlacher, J. Mugnier, J. Raman Spectrosc. 27 (1996) 785.
[8] Kunie. Ishioka, Hrvoje. Petek, Phys. Rev. B 86 (2012) 205201.
[9] C.J. Barbe, F. Arendse, P. Comte, M. Jirousek, M. Gratzel, J. Am. Ceram. Soc. 80 (1997) 3157.
[10] N. Kopidakis, K.D. Benkstein, J. van de Lagemaat, A.J. Frank, J. Phys. Chem. B 107 (2003) 11307.
[11] A.N.M. Green, E. Palomares, S.A. Haque, J.M. Kroon, J.R. Durrant, J. Phys. Chem. B 109 (2005) 12525.
[12] J. Nelson, S.A. Haque, D.R. Klug, J.R. Durrant, Phys. Rev. B 63 (2001) 205321.
[13] H. Tang, F. Levy, H. Berger, P.E. Schmid, Phys. Rev. B 52 (1995) 7771.
[14] H. Tang, H. Berger, P.E. Schmid, F. Levy, G. Burri, Solid State Commun. 87 (1993) 847.
[15] H. Tang, H. Berger, P.E. Schmid, F. Levy, Solid State Commun. 92 (1994) 267.
[16] W.F. Zhang, M.S. Zhang, Z. Yin, Phys. Status Solidi A 179 (2000) 319.
[17] L. Cavigli, F. Bogani, A. Vinattieri, V. Faso, G. Baldi, J. Appl. Phys. 106 (2009) 053516.
[18] L. Forss, M. Schubnell, Appl. Phys. B 56 (1993) 363.
[19] A. Maurya, P. Chauhan, S.K. Mishra, R.K. Srivastava, J. Alloys Compd. 509 (2011) 8433.
[20] C.C. Mercado, F.J. Knorr, J.L. McHale, S.M. Usmani, A.S. Ichimura, L.V. Saraf, J. Phys. Chem. C 116 (2012) 10796.
[21] F.J. Knorr, C.C. Mercado, J.L. McHale, J. Phys. Chem. C 112 (2008) 12786.
[22] J. Steckl, J.H. Park, J.M. Zavada, Prospects for rare earth doped GaN lasers on Si, Mater. Today 10 (2007) 20.
[23] M. Godlewski, M. Leskelea, Crit. Rev. Solid State Mater. Sci. 19 (1994) 199.
[24] H. Ennen, J. Schneider, G. Pomrenke, A. Axmann, Appl. Phys. Lett. 43 (1983) 943.
[25] H. Ennen, G. Pomrenke, A. Axmann, K. Eisele, W. Haydl, J. Schneider, Appl. Phys. Lett. 46 (1985) 381.
[26] A.-W. Xu, Y. Gao, H.-Q. Liu, J. catalysis 207 (2) (2002) 151.
[27] V. Stengl, S. Bakardjieva, N. Murafa, Mater. Chem. Phys. 114 (2009) 217.
[28] J. Liqiang, S. Xiaojun, X. Baifu, W. Baiqi, C. Weimin, F. Honggang, J. Solid State Chem. 177 (2004) 3375.
[29] M. Pal, U. Pal, J.M.G.Y. Jimenez, F. Perez-Rodríguez, Nanoscale Res. Lett. 7 (2014) 1.
[30] X. Chen, Wenqin Luo, J. Nanosci. Nanotechn. 10 (2010) 1482.
[31] B.H. Tong, S.J. Wang, Y.Z. Meng, B. Wang, Photochem. Photobiol. Sci. 6 (2007) 519.
[32] P. Kumar, H.K. Malik, A. Ghosh, R. Thangavel, K. Asokan, Appl. Phy. Lett. 102 (2013) 221903.
[33] J.F. Moulder, W.F. Strickle, P.E. Sobol, K.D. Bomben, Handbook of X-ray Photoelectron Spectroscopy, ULVAC-PHI Inc.
[34] A. Sandell, M.P. Andersson, Y. Alfredsson, M.K.J. Johansson, J. Schadt, H. Rensmo, H. Siegbahn, P. Uvdal, J. Appl. Phys. 92 (6) (2002) 3381.
[35] A. Sandell, M.P. Andersson, M.K.J. Johansson, P.G. Karlsson, Y. Alfredsson, J. Schadt, H. Siegbahn, P. Uvdal, Surf. Sci. 530 (12) (2003) 63.
[36] P. Stefanov, M. Shipochka, P. Stefchev, Z. Raicheva, V. Lazarova, L. Spassov, J. Phys: Conf. Ser. 100 (2008) 012039.
[37] Z. Song, J. Hrbek, R. Osgood, Nano Lett. 5 (7) (2005) 1327.
[38] N.D. Abazovic, L. Mirenghi, I.A. Jankovic, N. Bibic, D.V. Sojic, B.F. Abramovic, M.I. Comor, Nanoscale Res. Lett. 4 (2009) 518.
[39] G. Yang, Z. Jiang, H. Shi, T. Xiao, Z. Yan, J. Mater. Chem. 20 (2010) 5301.
[40] Vinod Kumar, V. Kumar, S. Som, J.H. Neethling, M. Lee, O.M. Ntwaeaborwa, H.C. Swart, Nanotechnology 25 (2014) 135701.
[41] Vinod Kumar, H.C. Swart, O.M. Ntwaeaborwa, R.E. Kroon, J.J. Terblans, S.K.K. Shaat, A. Yousif, M.M. Duvenhage, Mater. Lett. 101 (2013) 57.
[42] L. Yang, Y. Li, Y. Xiao, C. Ye, L. Zhang, Chem. Lett. 34 (2005) 828.
[43] L.-B. Xiong, J.-L. Li, B. Yang, Y. Yu, J. Nanomaterials 831524 (2012) 13.
[44] A. Fujishima, T.N. Rao, D.A. Tryk, J. Photochemistry and Photobiology C 1 (1) (2000) 1.
[45] Vinod Kumar, N. Singh, V. Kumar, L.P. Purohit, A. Kapoor, O.M. Ntwaeaborwa, H.C. Swart, J. Appl. Phys. 114 (2013) 134506.
[46] L. Kernazhitsky, V. Shymanovska, T. Gavrilko, V. Naumov, L. Fedorenko, V. Kshnyakin, J. Baran, Ukr. J. Phys. 59 (3) (2014) 246.
[47] A.G. Agrios, K.A. Gray, Langmuir 19 (2003) 1402.
[48] D. Pan, N. Zhao, Q. Wang, Adv. Mater. 17 (2005) 1991.
[49] A. Konrad, U. Herr, R. Tidecks, J. Appl. Phys. 90 (2001) 3516.
[50] A.S. Pereira, M. Peres, M.J. Soares, E. Alves, A. Neves, T. Monteiro, T. Trindade, Nanotechnol. 17 (2006) 834.
[51] S.S. Pitale, Vinay Kumar, I. Nagpure, O.M. Ntwaeaborwa, H.C. Swart, Current Appl. Phys. 11 (2011) 341.
[52] G.A. Kumar, M. Pokhrela, A. Martinez, R.C. Dennis, I.L. Villegas, D.K. Sardara, J. Alloys Compd. 513 (2012) 559.
[53] A.S. Pereira, M. Peres, M.J. Soares, E. Alves, A. Neves, T. Monteiro, T. Trindade, Nanotechnology 17 (2006) 834.